

Intensity adaptive optics

Zimo Zhao^{1,†}, Yifei Ma^{1,†}, Jacopo Antonello¹, Zipei Song¹, Jiahe Cui¹, Binguo Chen², Jingyu Wang¹, Bangshan Sun¹, Honghui He², Lin Luo³, Julian A.J. Fells¹, Steve J. Elston¹, Martin J. Booth¹, Stephen M. Morris¹, and Chao He^{1,*}

¹Department of Engineering Science, University of Oxford, Parks Road, Oxford, OX1 3PJ, UK

²Guangdong Engineering Center of Polarization Imaging and Sensing Technology, Tsinghua Shenzhen International Graduate School, Tsinghua University, Shenzhen 518055, China

³College of Engineering, Peking University, Beijing 100871, China

[†]These authors contributed equally to this work

*Corresponding author: chao.he@eng.ox.ac.uk

Adaptive optics (AO) is a powerful tool used in a wide range of research areas spanning from aerospace to microscopy. To date, AO has largely been applied to optical phase aberration correction, with recent advances extending to include the vectorial properties of light. However, intensity errors widely exist in optical systems, yet their associated correction methods are still very much in their infancy. Here, we propose a new adaptive optics method that is termed intensity adaptive optics (I-AO), which features a dual-feedback loop for intensity aberration correction that addresses both intensity uniformity and the overall intensity. We demonstrate that I-AO can operate in both sensor-based and sensorless regimes and validate its feasibility by quantitatively analysing the quality of the focus of an aberrated optical system. This technique expands the AO toolkit, broadens its scope of application, and opens a new avenue for next-generation AO innovations.

Introduction

Optical aberrations, including intensity, phase, and polarisation, compromise the performance of optical systems¹⁻⁴. For decades, adaptive optics (AO) has been a crucial technology in mitigating phase aberrations, thereby boosting the performance of astronomical telescopes⁵⁻⁷, optical communications⁸⁻¹⁰, and super-resolution microscopy/nanoscopy¹¹⁻¹⁷. Recently, AO has expanded into the vectorial domain, targeting either polarisation aberration alone (known as polarisation adaptive optics (P-AO)¹⁸⁻²²) or the combination of polarisation and phase aberrations (referred to as vectorial adaptive optics (V-AO)²³⁻²⁵). However, tools for correcting intensity aberrations remain undeveloped. We note that in various modern optical systems, intensity errors adversely affect performance, manifesting as non-uniform intensity distributions and energy loss. These errors can be attributed to the light source beam propagation^{26,27}, diattenuation effects^{23,28}, or absorption by materials or biological tissues²⁹⁻³³. In microscopy, for instance, these issues disrupt the intensity uniformity across the pupil of the objective lens, compromising overall system performance.

Intensity aberrations in optical systems often result in an aberrated focal spot. Image resolution is degraded due to imperfect interference and contrast is reduced due to energy loss, in turn lowering the signal-to-noise ratio (SNR) of resultant images³⁴. Degradation in both resolution and SNR critically undermine the effectiveness and data quality of the imaging process. Therefore, a correction technique targeting intensity aberration is essential. This will offer a significant enhancement to the existing AO toolkit.

In this work, we propose the concept of intensity adaptive optics (I-AO), highlighting a dual-loop feedback mechanism for intensity error correction in both sensor-based and sensorless formats. This concept focuses on correcting intensity variations at the pupil plane, which cannot be easily achieved by polarisation modulation at the image plane through the relation between polarisation and intensity. The concept of aberrations is illustrated in **Figure 1(a)**. **Figure 1(b)** and **Figure 1(c)** depict the schematic layout of the optical system before and after integration of the I-AO correction module, showing the achieved focus correction. The I-AO correction module consists of a spatial light modulator (SLM) sandwiched between two crossed polarisers for pixelated control of intensity across the beam transverse plane, as shown in **Figure 1(d)**. This configuration, previously utilised in structured light fields for beam modulation^{20,35}, is adapted here as an I-AO corrector for intensity errors. Additionally, an extra AO device, a deformable mirror (DM), is positioned next to the SLM-based module to

compensate for geometrical phase effects created by the SLM itself during the intensity correction process^{24,36}, as well as residual phase errors introduced by the optical system (see **Figure 1(d)**). We validated the feasibility of the proposed I-AO method by demonstrating the enhancement of both focus quality and intensity values following the correction of an intensity aberrated focusing system. Note that in all I-AO experiments conducted in this work, we introduced an additional correction routine to compensate for energy loss, beyond the standard correction loop for beam uniformity, by adjusting the attenuation filter after the laser to modify the overall intensity value. Further details are provided in **Supplementary Note 1**.

Overall, we demonstrate that I-AO effectively compensates for intensity aberrations, thus enhancing the existing AO technology toolkit. Notably, this advancement is particularly advantageous for applications requiring precise absolute intensity levels and uniform intensity at the pupil plane, such as pathology and clinical diagnostics³⁷.

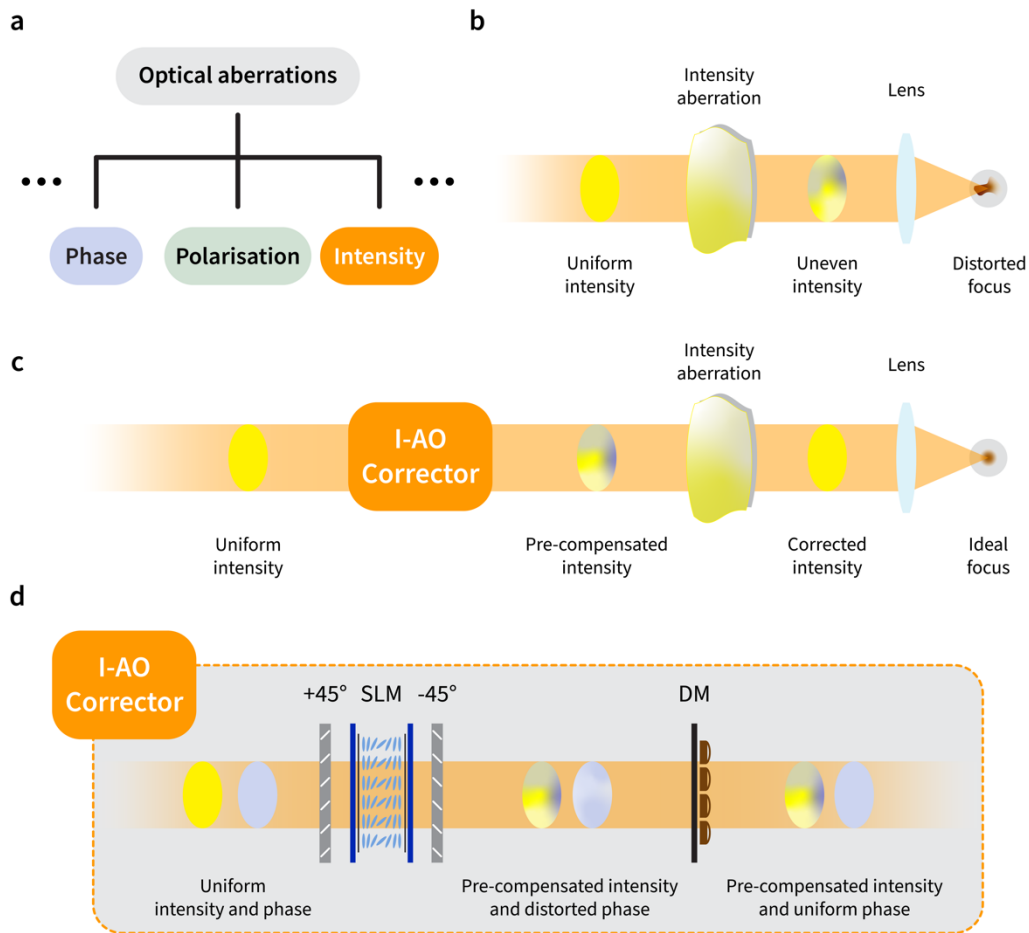


Figure 1 The concept of I-AO. **(a)** The performance of an optical system can be affected by different types of aberrations, such as phase, polarisation, intensity, etc. **(b)** An optical system compromised by intensity aberrations, as illustrated by the distorted focal spot. **(c)** The effect of integrating an I-AO corrector into the same system, where the aberrated focal spot is corrected to achieve an ideal focus. **(d)** Detailed arrangement of the I-AO corrector, highlighting how pixelated intensity correction is facilitated by sandwiching a spatial light modulator (SLM) between a pair of crossed polarisers. Additionally, an extra deformable mirror (DM) is incorporated to compensate any phase errors that arise during the intensity correction process, ensuring comprehensive aberration correction.

Results

Contrary to conventional AO techniques that assess phase and/or polarisation aberrations at the pupil plane, I-AO demands a comprehensive evaluation of the intensity variation across the pupil plane, achievable through either direct measurement or indirect estimation (e.g., image-based optimisation of focal quality). Therefore,

we propose two distinct I-AO methods for different imaging applications. The first approach involves direct sensing using an aberration sensor, referred to as sensor-based AO. The second approach relies on indirect optimisation, known as sensorless AO^{16,24,38}. Further elaboration and validation of both approaches are discussed in subsequent sections. For both I-AO methods (sensor-based and sensorless), two important points are emphasised. First, these methods combine the correction of both phase and intensity aberrations, addressing any additional phase errors induced by the AO device itself (geometrical effects) during the correction process. Second, the methods extend beyond the single-loop feedback mechanism of conventional AO to incorporate a dual-loop feedback correction process. Note that in conventional AO, correction typically relies on a single feedback loop that utilizes either direct measurements at the pupil plane or inferences of aberrations from focus intensity distributions at the focal plane, suitably adjusting the AO corrector to compensate for aberrations..

Sensor-based I-AO

The sensor-based I-AO approach involves the following pipeline: 1) An intensity sensor, such as a monochrome camera, first acquires a reference frame by capturing the full intensity profile of the SLM in its flat state where the light through the SLM has a uniform intensity distribution with no intensity aberrations. This intensity profile is taken at a plane corresponding to the conjugate pupil plane of the objective lens in the aberrated imaging system. Details of how to calibrate the flat state of the SLM-based corrector, the relationship between SLM retardance and I-AO corrector intensity values, as well as the intensity compensation algorithm are discussed in detail in **Supplementary Note 2**. 2) The distorted intensity profile in the presence of intensity aberrations is then measured to serve as feedback data. 3) The retardance values required for intensity pre-compensation is then calculated at the conjugate plane of the I-AO corrector to facilitate the first feedback correction loop (S1 in **Figure 2(a)**). 4) These retardance values are applied to the I-AO corrector to achieve uniform intensity across the pupil. 5) The DM is further used to perform sensorless AO and compensate for both the geometrical phase aberrations induced by the SLM itself, and the systematic phase errors throughout the system. 6) With a uniform intensity profile obtained at the focal plane, the attenuator after the light source is finally adjusted based on the reference data to enhance the total intensity value, marking the end of the second feedback loop (S2 in **Figure 2(a)**). Details of the sensor-based dual-loop feedback correction algorithm are elaborated in **Supplementary Note 3**. This methodology was validated through two experiments to showcase its viability.

Our first experiment demonstrated the necessity of I-AO. Initially, we introduced an external spatially varying intensity aberration to an optical focusing system (see **Figure 2(b)**, I-AO off) and attempted sensorless phase AO correction via the DM (see **Figure 2(b)**, Phase AO on). The results showed a persistent focus aberration, indicating that conventional phase AO correction cannot fully rectify intensity aberrations due to their impact on interference in the focal plane, and results in an imperfect focal spot. After removing the intensity aberration, the original intensity distribution was restored across the pupil to achieve a diffraction-limited focal spot. **Figure 2(c)** plots the intensity values across a cross-section of the focal spot for each step. Validation confirms that I-AO is essential for complete intensity aberration correction. This outcome indicates that once system aberrations are addressed with phase AO, any remaining distortions in the intensity profile are attributable to intensity aberrations introduced during the experiment.

In our second experiment, we performed sensor-based I-AO correction for the same intensity aberration as in the first experiment, with pupil and focal plane profiles depicted in **Figure 2(d)** (I-AO off). Following the pipeline outlined earlier, after an attempt to correct using sensorless phase AO, the first feedback loop, S1, corrected the intensity profile based on the measured pupil image, resulting in a uniform intensity profile across the pupil as shown in **Figure 2(d)** (I-AO S1). Comparing the intensity profile along a cross-section of the focus before and after I-AO correction revealed enhanced pupil intensity uniformity and focal spot quality. Subsequently, sensorless phase AO was performed (see **Figure 2(d)**, Phase AO on) and feedback loop S2 was implemented (see **Figure 2(d)**, I-AO S2) for further improvements, with corresponding focal spot cross-sections illustrated in **Figure 2(e)** for each step.

The experiments above demonstrated that the sensor-based I-AO method featuring dual-loop feedback correction notably enhances the performance of an intensity-aberrated optical system by improving both the uniformity of the intensity as well as the total intensity.

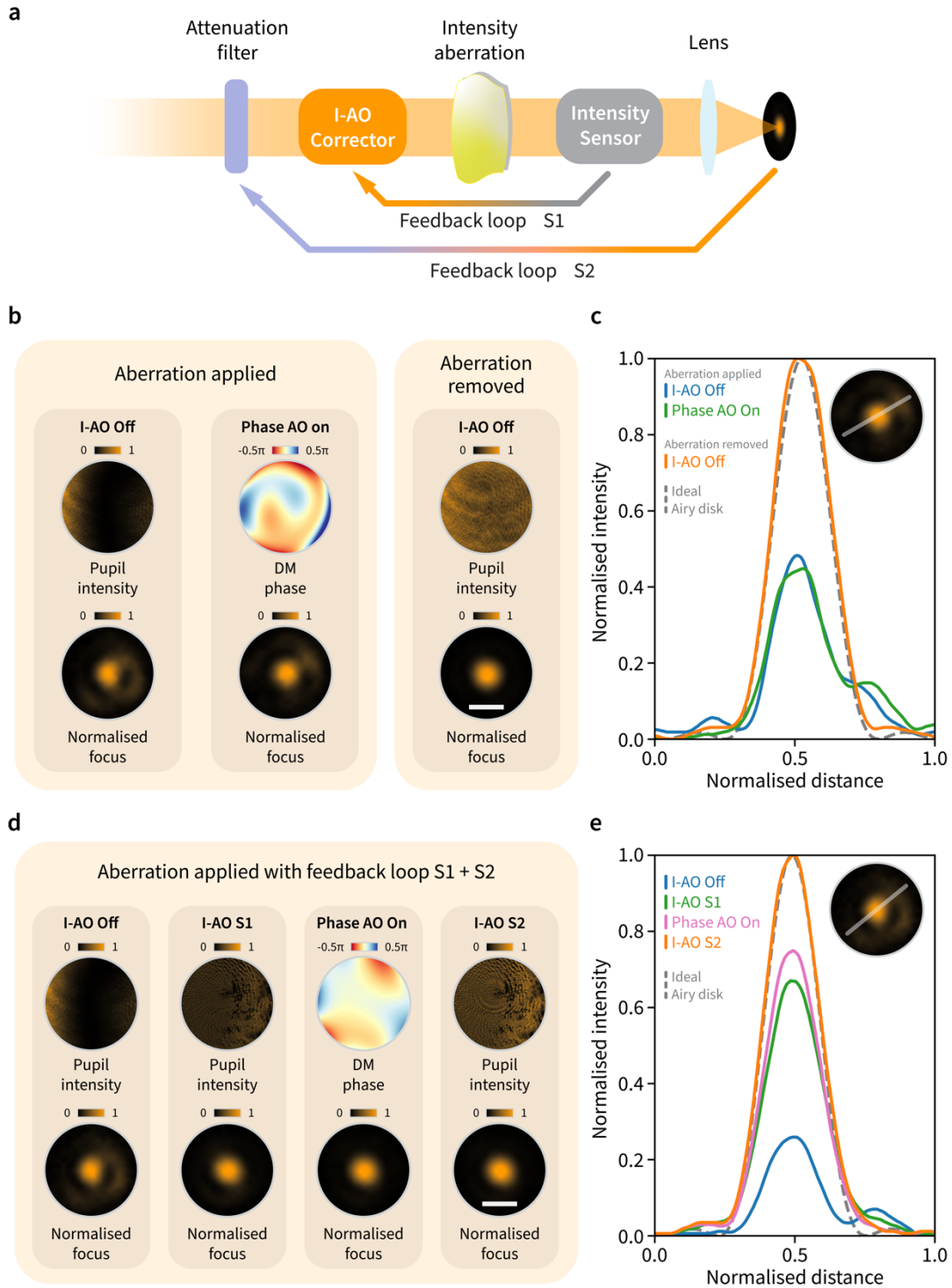


Figure 2 Sensor-based I-AO for intensity aberration correction. **(a)** Conceptual schematic of sensor-based I-AO with dual-loop feedback correction. The intensity sensor is utilised to measure the intensity variation directly from the pupil plane. **(b)** Demonstration of the necessity of I-AO for intensity aberration correction by comparison with the results of traditional phase AO correction. The intensity profile of the pupil, the phase applied to the DM and the profile of the focus are given, for the conditions of I-AO off (with intensity aberration applied), phase AO on, I-AO off (without intensity aberration applied), separately. **(c)** Intensity profile plots along a sampled cross-section of the focus for each step in (b). The profile of an ideal Airy disk is indicated with a dashed line. **(d)** Sensor-based I-AO correction for the intensity aberration in (b) with a dual feedback loop. The intensity profile of the pupil, the phase applied to the DM, and the profile of the focus for each step are given. **(e)** Intensity profile plots along a sampled cross-section of the focus for each step in (d) with a dual feedback loop. The profile of an ideal Airy disk is indicated with a dashed line. The scale bar (white solid bars in (b) and (d)) represents $30\ \mu\text{m}$ for all normalised focus images.

Sensorless I-AO

Here, we demonstrate the feasibility of the sensorless I-AO approach, eliminating the need for direct sensor-based measurement of intensity variation at the pupil plane, which is usually a challenging task in compact optical systems. Instead, this approach indirectly infers aberrations by analysing the image of the focal spot as feedback. Mimicking conventional phase AO, this method applies a series of pre-designed aberration correction patterns sequentially to the AO device, with the optimal correction determined by maximizing the image quality metric assessing the low spatial frequency content of the image³⁹ and the focal spot circularity (roundness). It is crucial to note that: 1) As intensity is a non-negative quantity, it is not possible to use conventional orthogonal Zernike modes as the basis for correction; 2) Similar to the sensorless technique in modern V-AO correction methods, the I-AO approach has to deal with the complex interplay between intensity and phase through geometrical links when modulating the SLM, suggesting the need for simultaneous correction of any additional phase errors introduced by the SLM during intensity aberration correction. Details on the concept of intensity-based Zernike modes, as well as their design and implementation, are available in **Supplementary Note 4**.

Sensorless I-AO deviates from traditional phase AO in the way that correction modes cannot be superimposed or adjusted with coefficients for optimization, otherwise the intensity may be saturated. Considering this power-related nature, one single intensity Zernike mode along with its most optimal coefficient value will be chosen to compensate for the intensity aberration. The distinct steps include: 1) To begin with, 15 intensity Zernike modes will be interrogated and analysed, including four standard aberration modes typically not corrected for in conventional phase AO - piston, tip, tilt, and defocus; 2) Images of the focal spot are recorded for each intensity Zernike mode applied at different amplitudes. By contrast to conventional phase AO that applies a combination of Zernike modes during aberration correction⁴⁰, each correction mode in I-AO is applied individually with a corresponding coefficient; 3) Finally, two image metrics, the low spatial frequency content of the captured image and spot circularity are used to find the best focus profile, ultimately determining the optimal intensity Zernike mode and coefficient value for correction. See **Supplementary Note 5** for the detailed mechanism.

We conducted experiments to validate the sensorless I-AO approach, employing the same external intensity aberration as that used during sensor-based I-AO validation. **Figure 3(a)** demonstrates the sensorless I-AO procedure. The approach is similar to that of the sensor-based method, as it also utilises a dual-loop feedback loop, but in this case, it relies on the image of the focal spot to infer the aberration indirectly instead of directly measuring the intensity profile at the pupil for correction feedback. **Figure 3(b)** shows the results for each step of correction. Initially, the intensity aberration creates an irregular focal spot (see **Figure 3(b)**, I-AO off). Conventional sensorless phase AO is first applied to address the phase errors introduced by optical components in the system, with the applied correction phase pattern and post-correction focal image shown in **Figure 3(b)** (Phase AO on). Following this, sensorless I-AO scans through a pre-determined set of intensity Zernike modes, identifying the optimal SLM phase pattern composed of the best intensity Zernike mode and corresponding coefficient that yields the highest image metric. The shape of the restored focal spot is demonstrated in **Figure 3(b)** (I-AO SL1). Conventional sensorless phase AO then further corrects for residual phase errors and enhances intensity uniformity. The final DM phase pattern and resulting focal spot image are shown in **Figure 3(b)** (Phase AO on). Finally, feedback loop SL2 compensates for total intensity loss (see **Figure 3(b)**, I-AO SL2), with the intensity profile plots along a cross-section of each focal spot displayed in **Figure 3(c)**. Comparing the beam intensity level and profile between the ideal and corrected focal spots reveal a clear improvement in the quality of the intensity profile during the sensorless I-AO correction steps.

The measurement results confirm the potential of sensorless I-AO for future applications that require both intensity and phase correction. This is particularly significant for situations where the integration of extra hardware to directly measure intensity aberrations is constrained and highlights the importance of indirect optimisation for compact optical imaging systems.

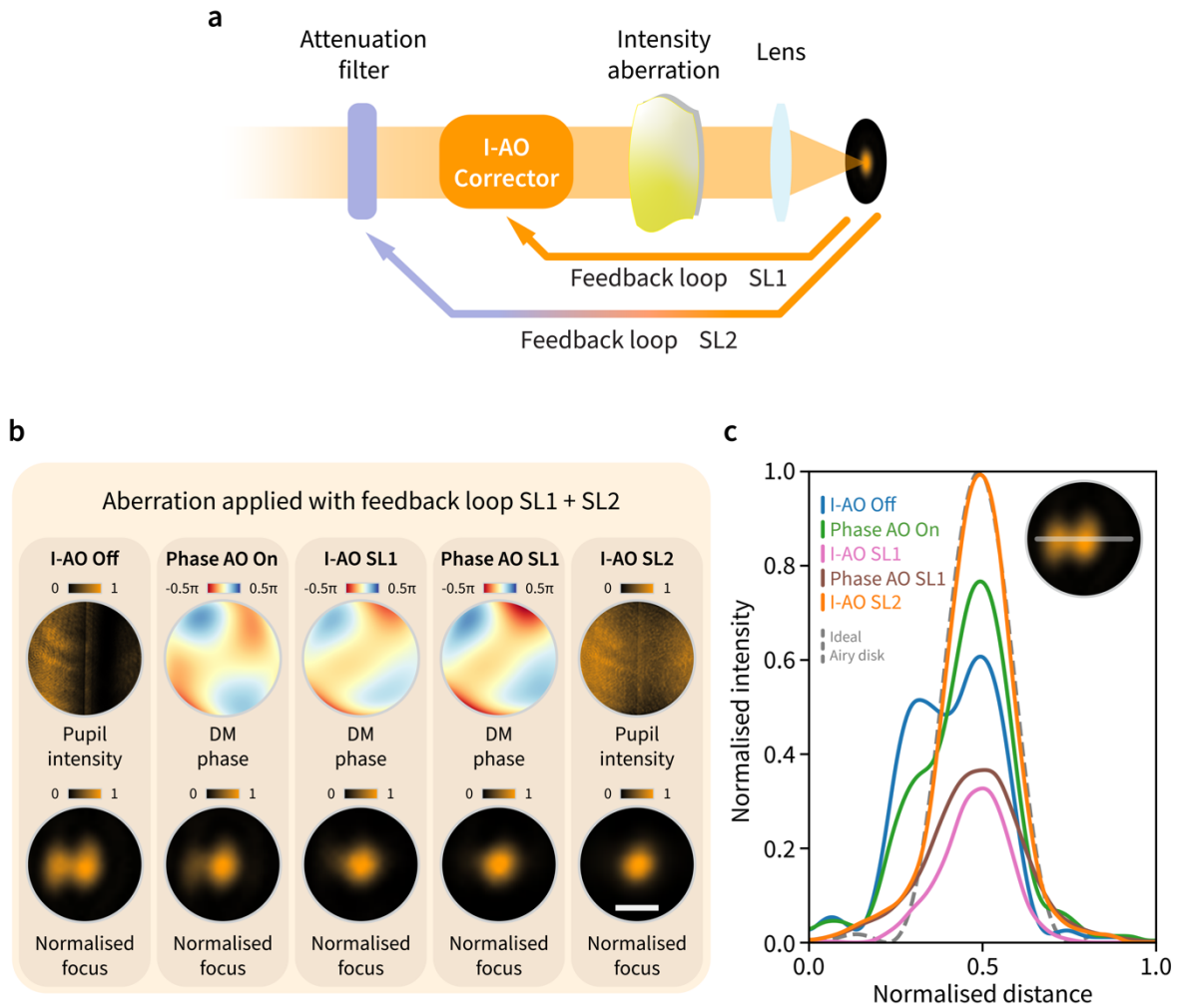


Figure 3 Sensorless I-AO for intensity aberration correction. **(a)** A schematic illustration of the concept of sensorless I-AO for intensity aberration correction with dual-loop feedback correction. **(b)** Sensorless I-AO correction procedure for intensity aberrations with dual-loop feedback. The intensity profile of the pupil, the phase applied to the DM and the intensity profile of the focus are given, for the conditions of I-AO off, phase AO on, I-AO SL1, Phase AO SL1, and I-AO SL2, separately. **(c)** Composite plot of intensity profiles along a sampled cross-section of the focus for each step during sensorless I-AO correction. The intensity of an ideal Airy disk is shown by the dashed line. The scale bar (white solid bar in (b) and (d)) represents $30\ \mu\text{m}$ for all normalised focus images.

Discussions

In summary, I-AO introduces novel concepts to correct for intensity aberrations that can be implemented via dual-loop feedback. This includes a sensor-based format, which directly measures intensity aberrations from the pupil plane, and a sensorless format that utilises innovative intensity modes and associated sensorless processes to indirectly infer aberrations from the focal spot.

These two approaches offer a versatile toolkit for intensity aberration correction across various optical systems, benefitting real-world applications. Sensor-based I-AO enables direct visualisation and compensation of the intensity profile, allowing for efficient and precise intensity manipulation and correction. In this work, we focus solely on intensity, using a camera as the primary sensor, with residual phase errors addressed through sensorless AO. In future developments, we expect to integrate a Shack-Hartmann wavefront sensor for precise geometrical phase measurement to enhance correction accuracy. The sensorless I-AO approach also presents significant potential for exploration. In this work, we designed intensity Zernike modes that are based on conventional

Zernike modes used in phase AO. However, these intensity Zernike modes are not the best set of modes to use for sensorless I-AO correction because they are not orthogonal and do not support super-positioning as intensity is a non-negative quantity; therefore, they are used primarily for conceptual demonstration purposes. For instance, zonal correction^{41,42} or other novel intensity modes may offer better alternatives than Zernike modes⁴⁰ for enhancing correction accuracy and precision and could be more effective for sensorless I-AO correction.

Future work could explore the development of new image metrics and improved sensorless I-AO processes, possibly leveraging cutting-edge machine learning techniques^{2,43,44}. Additionally, integrating the I-AO toolkit with V-AO and spatiotemporal control^{44,46} will facilitate comprehensive field correction and particularly benefit complex optical systems and applications⁴⁷⁻⁵⁰.

Overall, we have introduced novel I-AO techniques for correcting intensity aberrations by employing a dual-loop feedback mechanism for intensity control. By addressing the challenge of intensity aberration correction, this approach substantially enhances the performance of optical systems and boosts current capabilities of current AO systems. This advanced AO approach promises significant impacts across various research fields, from enhancing astronomical telescope technology for detailed studies of galaxies to improving microscopy for sharper clinical diagnostics. The approach is particularly beneficial for applications where absolute intensity levels are critical to the imaging result, such as in the pathology of human retinal diseases⁵¹.

References

- [1] Booth, M. J. Adaptive optics in microscopy. *Phil. Trans. R. Soc. A* **365**, 2829–2843 (2007).
- [2] Hampson, K.M. *et al.* Adaptive optics for high-resolution imaging. *Nat. Rev. Methods Primers* **1**, 68 (2021).
- [3] Shen, Y., Chen, B., He, C. *et al.* Polarization Aberrations in High-Numerical-Aperture Lens Systems and Their Effects on Vectorial-Information Sensing. *Remote Sens.* **14**, 1932 (2022).
- [4] He, C., Antonello, J. & Booth, M.J. Vectorial adaptive optics. *eLight* **3**, 23 (2023).
- [5] Roddier, F. *Adaptive Optics in Astronomy* (Cambridge Univ. Press, 1999).
- [6] Rigaut, F. & Neichel, B. Multiconjugate Adaptive Optics for Astronomy. *Annu. Rev. Astron. Astrophys.* **56**, 277–314 (2018).
- [7] Do, T., Hees, A., Ghez, A. *et al.* Relativistic redshift of the star S0-2 orbiting the Galactic Center supermassive black hole. *Science* **365**, 664–668 (2019).
- [8] Jian, H., Ke, D., Chao, L. *et al.* Effectiveness of adaptive optics system in satellite-to-ground coherent optical communication. *Opt. Express* **22**, 16000 (2014).
- [9] Liu, C., Chen, M., Chen, S. *et al.* Adaptive optics for the free-space coherent optical communications. *Opt. Commun.* **361**, 21–24 (2016).
- [10] Zhang, S. *et al.* Extending the detection and correction abilities of an adaptive optics system for free-space optical communication. *Opt. Commun.* **482**, 126571 (2021).
- [11] Porter, J. *Adaptive optics for vision science*. (Wiley-Interscience, 2006).
- [12] Vangindertael, J., Camacho, R., Sempels W. *et al.* An introduction to optical super-resolution microscopy for the adventurous biologist. *Methods Appl. Fluores.* **6**, 022003 (2018).
- [13] Ji, N., Sato, T. R. & Betzig, E. Characterization and adaptive optical correction of aberrations during in vivo imaging in the mouse cortex. *Proc. Natl Acad. Sci. USA* **109**, 22–27 (2012).
- [14] Kubby, J. A. *Adaptive optics for biological imaging* (Taylor & Francis, 2013).
- [15] Booth, M. Adaptive optical microscopy: the ongoing quest for a perfect image. *Light Sci. Appl.* **3**, e165 (2014).
- [16] Ji, N. Adaptive optical fluorescence microscopy. *Nat Methods* **14**, 374–380 (2017).
- [17] Liu, R., Li, Z., Marvin, J.S. *et al.* Direct wavefront sensing enables functional imaging of infragranular axons and spines. *Nat Methods* **16**, 615–618 (2019).
- [18] Chipman, R. A. & Chipman, L. J. Polarization Aberration Diagrams. *Optical Engineering* **28**, 282100 (1989).
- [19] Dai, Y. He, C. Wang, J. *et al.* Active compensation of extrinsic polarization errors using adaptive optics. *Opt. Express* **27**, 35797 (2019).
- [20] Hu, Q., He, C., & Booth, M. J. Arbitrary complex retarders using a sequence of spatial light modulators as the basis for adaptive polarisation compensation. *J. Opt.* **23**, 065602 (2021).
- [21] He, C., He, H., Chang, J. *et al.* Polarisation optics for biomedical and clinical applications: a review. *Light Sci. Appl.* **10**, (2021).

- [22] He, C. & Booth, M. J. Improvement of resolution and polarisation measurement precision in biomedical imaging through adaptive optics. *Polarized Light in Biomedical Imaging and Sensing* **13** 345–360 (2022).
- [23] He, C. & Booth, M. J. Vectorial adaptive optics: Correction of polarization and phase. *Imaging and Applied Optics Congress 2022 (3D, AOA, COSI, ISA, pcAOP)* (2022).
- [24] He, C., Chen, B. Song, Z., *et al.* A universal optical modulator for synthetic topologically tuneable structured matter. Preprint at <https://doi.org/10.48550/arXiv.2311.18148> (2023).
- [25] Ma, Y., Zhao, Z., Cui, J. *et al.* Vectorial adaptive optics for advanced imaging systems. *J. Opt.* **26**, 065402 (2024)
- [26] Booth, M.J., Andrade, D., Burke, D. *et al.* Aberrations and adaptive optics in super-resolution microscopy. *Microscopy* **64**, 251–261 (2015).
- [27] Lukin, V. P. Adaptive optics in the formation of optical beams and images. *Phys.-Usp.* **57**, 556–592 (2014).
- [28] Anche, R. M., Ashcraft, J. N., Haffert, S. Y. *et al.* Polarization aberrations in next-generation Giant Segmented Mirror Telescopes (GSMTs). *A&A* **672**, A121 (2023).
- [29] Wang, C., Liu, R., Milkie, D. E. *et al.* Multiplexed aberration measurement for deep tissue imaging in vivo. *Nat. Methods* **11**, 1037–1040 (2014).
- [30] Wang, K., Sun, W., Richie, C. T. *et al.* Direct wavefront sensing for high-resolution in vivo imaging in scattering tissue. *Nat. Commun.* **6**, 7276 (2015).
- [31] Bisch, N., Guan, J., Booth, M.J. *et al.* Adaptive optics aberration correction for deep direct laser written waveguides in the heating regime. *Appl. Phys. A* **125**, 364 (2019).
- [32] Salter, P.S., Booth, M.J. Adaptive optics in laser processing. *Light Sci. Appl.* **8**, 110 (2019).
- [33] Lin, R., Kipreos, E.T., Zhu, J. *et al.* Subcellular three-dimensional imaging deep through multicellular thick samples by structured illumination microscopy and adaptive optics. *Nat. Commun.* **12**, 3148 (2021).
- [34] Welford, W. T. *Aberrations of Optical Systems* (CRC Press LLC, 2017).
- [35] Hu, Q., Dai, Y., He, C. *et al.* Arbitrary vectorial state conversion using liquid crystal spatial light modulators. *Opt. Commun.* **459**, 125028 (2020).
- [36] He, C., Shen, Y. & Forbes, A. Towards higher-dimensional structured light. *Light Sci. Appl.* **11**, 205 (2022).
- [37] Lee, K. E., Heitkotter, H., Carroll, J. Challenges Associated With Ellipsoid Zone Intensity Measurements Using Optical Coherence Tomography. *Trans. Vis. Sci. Tech.* **10**, 27 (2021)
- [38] Booth, M. J. Wavefront sensorless adaptive optics for large aberrations. *Opt. Lett.* **32**, 5-7 (2007)
- [39] Debarre, D., Booth, M. J. & Wilson, T. Image based adaptive optics through optimisation of low spatial frequencies. *Opt. Express* **15**, 8176 (2007).
- [40] Lakshminarayanan, V. & Fleck, A. Zernike polynomials: a guide. *J. Mod. Opt.* **58**, 545–561 (2011).
- [41] Prengère, L., Kulcsár, C. & Raynaud, H.-F. Zonal-based high-performance control in adaptive optics systems with application to astronomy and satellite tracking. *J. Opt. Soc. Am. A* **37**, 1083 (2020).
- [42] Zhang, B., Zhu, J., Si, K. *et al.* Deep Learning Assisted Zonal Adaptive Aberration Correction *Front. Phys.* **8**, (2021).

- [43] Hu, Q., Hailstone, M., Wang, J. *et al.* Universal adaptive optics for microscopy through embedded neural network control. *Light Sci. Appl.* **12**, 270 (2023).
- [44] Zhang, Q., Hu, Q., Berlage, C. *et al.* Adaptive optics for optical microscopy [Invited]. *Biomed. Opt. Express* **14**, 1732 (2023).
- [45] Yao, P., Liu, R., Brogini, T. M. *et al.* Construction and use of an adaptive optics two-photon microscope with direct wavefront sensing. *Nat. Protoc.* **18**, 3732–3766 (2023).
- [46] Tang, J., Wu, J., Zhang, J. *et al.* Highly robust spatiotemporal wavefront prediction with a mixed graph neural network in adaptive optics. *Photonics Res.* **11**, 1802 (2023).
- [47] Khonina, S. N., Volotovskiy, S. G., Dzyuba, A. P. *et al.* Power Phase Apodization Study on Compensation Defocusing and Chromatic Aberration in the Imaging System. *Electronics* **10**, 1327 (2021).
- [48] He, C., Lin, J., Chang, J. *et al.* Full Poincaré polarimetry enabled through physical inference. *Optica* **9**, 1109 (2022).
- [49] He, C., Chang, J., Hu, Q. *et al.* Complex vectorial optics through gradient index lens cascades. *Nat. Commun.* **10**, 4264 (2019).
- [50] Ashida, Y., Honma, Y., Miura, N. *et al.* Imaging performance of microscopy adaptive-optics system using scene-based wavefront sensing. *J. Biomed. Opt.* **25**, 123707 (2020).
- [51] Ruminski, D., Sikorski, B. L., Bukowska, D. *et al.* OCT angiography by absolute intensity difference applied to normal and diseased human retinas. *Biomed. Opt. Express* **6**, 2738-2754 (2015)

Supplementary Information

Intensity adaptive optics

Zimo Zhao^{1,†}, Yifei Ma^{1,†}, Jacopo Antonello¹, Zipei Song¹, Jiahe Cui¹, Binguo Chen², Jingyu Wang¹, Bangshan Sun¹, Honghui He², Lin Luo³, Julian A.J. Fells¹, Steve J. Elston¹, Martin J. Booth¹, Stephen M. Morris¹, and Chao He^{1,*}

¹Department of Engineering Science, University of Oxford, Parks Road, Oxford, OX1 3PJ, UK

²Guangdong Engineering Center of Polarization Imaging and Sensing Technology, Tsinghua Shenzhen International Graduate School, Tsinghua University, Shenzhen 518055, China

³College of Engineering, Peking University, Beijing 100871, China

[†]These authors contributed equally to this work

*Corresponding author: chao.he@eng.ox.ac.uk

Supplementary Note 1:

Dual-loop correction approach in I-AO corrector

In conventional phase adaptive optics, correction typically relies on a single feedback loop that utilizes either direct wavefront measurements at the pupil plane (sensor-based) or infers phase aberrations from focus intensity distributions (sensorless) at the focal plane, suitably adjusting the AO corrector for phase aberrations. But this single feedback loop is insufficient for correcting intensity aberrations, which can alter the energy distribution and risk total energy loss. To overcome this limitation, we propose a dual-loop correction mechanism within the I-AO corrector system. The initial loop adheres to traditional phase AO correction principles, aiming to restore either intensity uniformity or focus shape without affecting the beam's total energy. Subsequently, the second loop addresses any energy deficiencies by modifying the beam's initial intensity. This dual-loop strategy effectively divides the intensity aberration correction process into two sub-tasks: intensity uniformity restoration and total intensity recovery, ensuring that no energy is sacrificed. **Figure S1** demonstrate this dual-loop correction approach in detail.

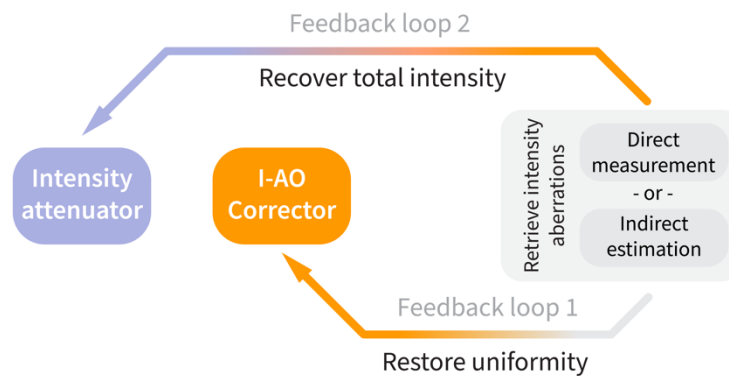


Figure S1: Dual-loop correction approach in I-AO. The first loop corrects phase aberrations, preserving beam energy, while the second loop addresses energy deficiencies, ensuring uniform intensity and total intensity recovery without energy loss.

Supplementary Note 2:

Spatial light modulator (SLM) calibration in an intensity adaptive optics (I-AO) corrector

An SLM is positioned in the I-AO corrector between two polarisers aligned at orthogonal angles. This configuration, with both polarisers aligned at a 45° angle to the nematic liquid crystal (NLC) within the SLM, facilitates pixelated intensity modulation through the NLC's Fréedericksz transition. The formula for the transmittance (T) of light through the NLC layer is

$$T = \sin^2(2\chi) \sin^2\left(\frac{\pi\Delta nd}{\lambda}\right) \quad (1)$$

where χ represents the 45° angle between the polariser and the NLC director, Δn denotes the NLC's birefringence, d represents the distance that light travels within the NLC layer, and λ is the wavelength.

Light intensity modulation in the I-AO corrector is achieved by controlling the voltage applied to the NLC within the SLM to change the birefringence. This is achieved using an 8-bit grayscale image of the same resolution as the SLM panel, which is further converted to voltages according to a manufacturer-defined grayscale-to-voltage map. However, the thickness of the NLC layer varies due to the uneven SLM surface, which impacts modulation efficiency. A pixel-specific look-up table (LUT) is therefore needed to account for these disparities. This LUT correlates pixel values with their modulated intensities, enabling precise and rapid intensity adjustments during the correction process by quickly identifying the appropriate pattern to load onto the SLM. The LUT for each SLM pixel is derived by mapping the intensity modulation to grayscale values. To achieve maximum dynamic range, the laser intensity is adjusted using a neutral density (ND) filter and the exposure time of a monochrome camera placed at the pupil plane is also optimised. These parameters then remain constant throughout the calibration routine.

Next, to efficiently capture intensity modulation responses across all SLM pixels, uniform images with a single value (termed flat value F_i) are applied to the SLM. With an 8-bit pixel modulation depth, flat values $F_i = i$ satisfying $i \in [0, 255]$, $i \in \mathbb{Z}$ are systematically tested for each SLM pixel. We apply the same flat value F_i to all N pixels of the SLM each time and incrementally increase the flat value of the uniform image from 0 to 255, in total capturing 256 images of the full SLM active region. It should be noted that the discrepancy between SLM resolution and camera sensor size is mitigated through interpolation. This ensures an accurate one-to-one mapping between each pixel on the SLM and each pixel on the camera image, and eliminates potential issues related to resolution mismatch. Consequently, an intensity response P_{n_i} is determined for every pixel n through the camera image corresponding to flat value F_i , and a modulation range $[P_{n_0}, P_{n_1}, \dots, P_{n_{255}}]$ is derived for each pixel n . This process records the modulation profile of the entire pixel space and enables precise calibration of pixel-specific intensity responses, which are typically represented by trigonometric functions within the modulation range¹.

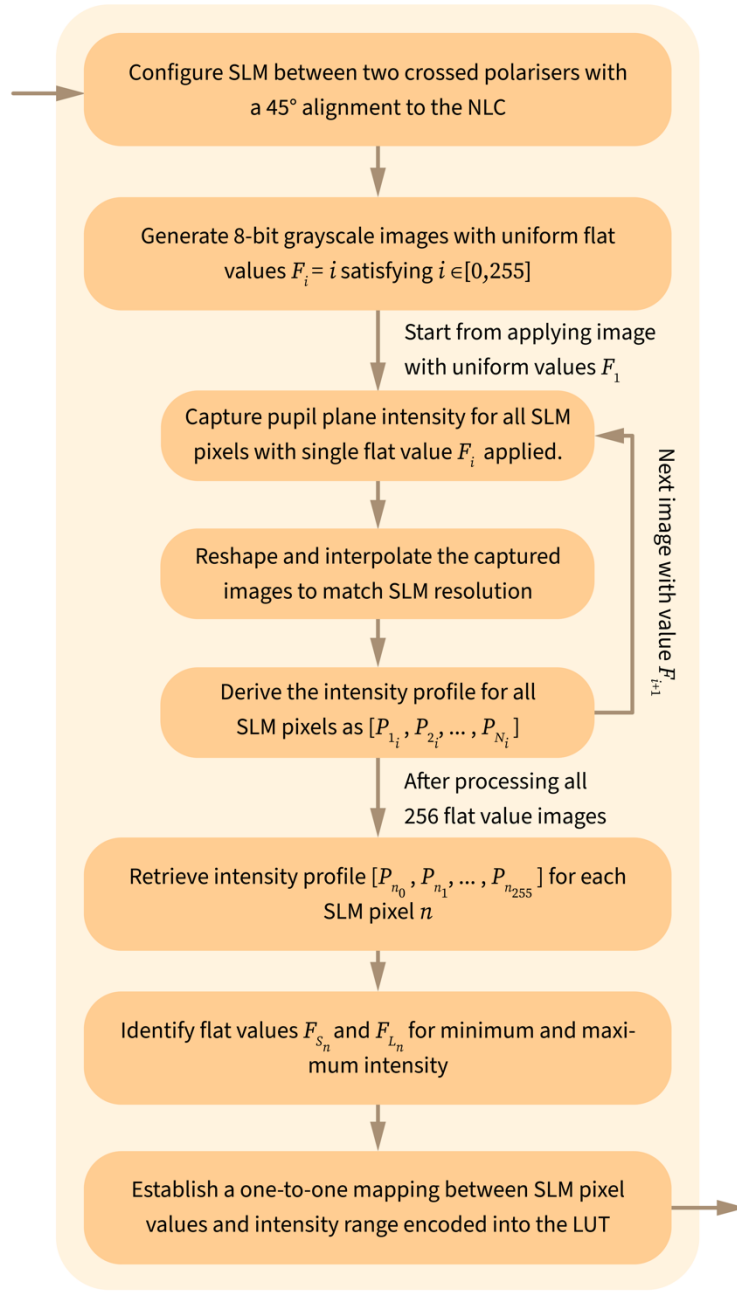


Figure S2: Flowchart illustrating the sequential steps involved in the calibration process of the SLM within the I-AO corrector, as comprehensively outlined in **Supplementary Note 2**. The configuration of the SLM during calibration, the measurement of the intensity modulation range for each pixel, and the generation of a pixel specific LUT for precise intensity correction is outlined.

To ensure the mapping is unique between SLM pixel values and intensity modulation, flat values F_{S_n} and F_{L_n} corresponding to minimum intensity $P_{n_{S_n}}$ and maximum intensity $P_{n_{L_n}}$ are identified for each SLM pixel n . Intensity values within the range of $P_{n_{S_n}}$ to $P_{n_{L_n}}$ and their corresponding flat values are used for I-AO compensation, with intensity values outside this range being discarded. Thus, for each SLM pixel index n , when its pixel value is set between F_{S_n} and F_{L_n} , it will have a one-to-one mapping to the range of intensity values

between $P_{n_{S_n}}$ to $P_{n_{L_n}}$ on the monochromatic camera. This approach establishes the relationship between flat values of each SLM pixel and the intensity values it can modulate for each SLM pixel through the I-AO corrector, which is then encoded into the LUT together with the valid pixel value range. This calibration methodology is detailed in the accompanying flowchart in **Figure S2**.

To achieve a desired output intensity using the I-AO corrector, each SLM pixel is systematically modulated by selecting a value F_i between F_{S_n} and F_{L_n} that generates a corresponding intensity P_{n_i} closely matching the target P_{n_T} on the monochrome camera according to the pre-calibrated LUT. Subsequently, conventional phase AO correction is applied using a single deformable mirror (DM) to correct for phase aberrations induced by the SLM and other system-specific optical phase aberrations. For a uniform output intensity, a single target intensity level P_{n_T} is set across the monochrome camera, which further validates the unique pattern on the SLM that ensures a uniform intensity at the pupil plane. In this case, the image (**Figure 2(b)** in the main manuscript) taken at the focal plane reveals an ideal focal intensity distribution resembling a standard Airy disk shape.

Supplementary Note 3:

Experimental procedures for sensor-based I-AO correction

Sensor-based I-AO directly measures aberrations at the pupil plane with a sensor. Initially, the SLM is set to a flat state (see **Supplementary Note 2**), and reference images are captured from both the pupil and focal planes. After that, the external intensity aberration is introduced into the system, and the distorted intensity profile at the pupil plane is captured by the intensity sensor, initiating a dual-feedback loop for sensor-based correction. Loop 1 recovers the intensity profile and calculates the intensity loss ΔP_n for each pixel n by comparing captured intensity values P_{n_c} with the target level P_{n_T} , where $\Delta P_n = P_{n_T} - P_{n_c}$. A new value $\tilde{P}_n = P_{n_T} + \Delta P_n$ is then set as the target intensity on the monochrome camera to compensate for the intensity aberration, leading to a new SLM pattern based on the pre-calibrated LUT. The corrected pupil intensity is further assessed to confirm optimal beam uniformity restoration. Finally, conventional phase AO correction is applied to address phase aberrations introduced by the SLM during intensity correction. The focus intensity distribution (FID) at the focal plane resembles that of an ideal Airy disk, also validating that the intensity profile at the pupil plane would be uniform.

After rectifying the uniformity of the intensity profile at the pupil plane and the FID profile at the focal plane in the first loop, the second loop focuses on recovering the total intensity of the initial beam by adjusting the attenuation filter at the illumination source with feedback of the intensity level measured by the camera. A flowchart in **Figure S3** outlines this sensor-based correction methodology.

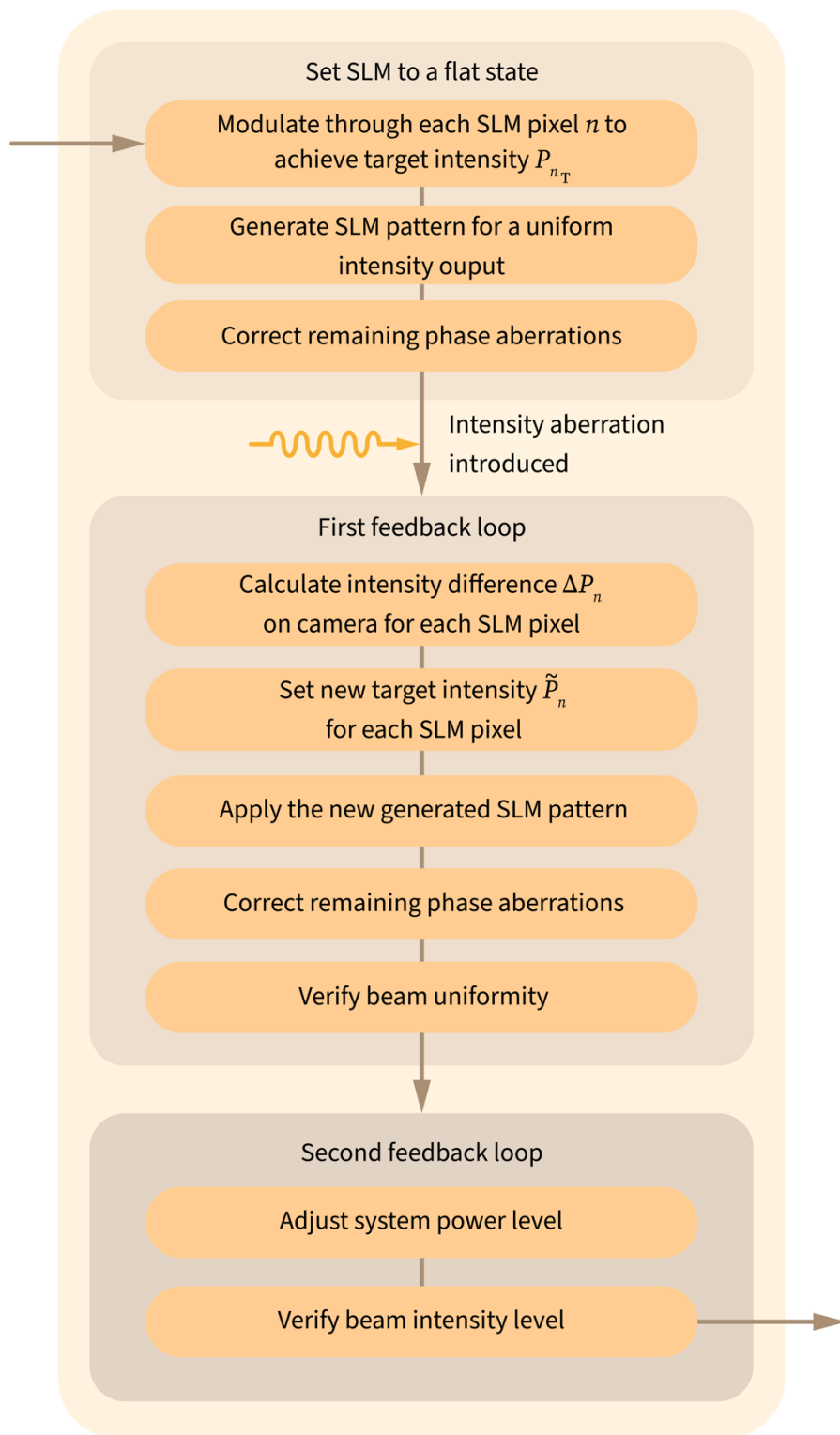


Figure S3: Flowchart outlining the sensor-based correction methodology. The critical steps include SLM flat state initialisation, beam uniformity restoration (loop 1), and total intensity recovery (loop 2). The dual feedback loop is highlighted for simultaneous beam uniformity restoration and total intensity recovery.

Supplementary Note 4:

Intensity Zernike Modes

Our proposed sensorless I-AO method infers and corrects for intensity aberrations by measuring the FID profile at the focal plane as feedback for the I-AO corrector, employing a correction mechanism similar to that of conventional sensorless phase AO. However, instead of using conventional phase AO Zernike modes, we introduce a modified set of Zernike modes to represent intensity aberrations. Recognising that intensity is a non-negative quantity, therefore modes that are also non-negative are required for the correction process., These modified Zernike modes differ in both the range of possible values and application strategy, and can be expressed as

$$Z_n^m(\rho, \theta) = \frac{1}{2} [c_n^m R_n^{|m|}(\rho) \Theta_n^m(\theta)] + \frac{1}{2} \quad (2)$$

where:

$$c_n^m = 1 \quad (3)$$

$$\Theta_n^m(\theta) = \begin{cases} \cos(m\theta) & m \geq 0 \\ -\sin(m\theta) & m < 0 \end{cases} \quad (4)$$

$$R_n^{|m|}(\rho) = \sum_{l=0}^{(n-|m|)/2} \frac{(-1)^l (n-l)!}{l! \left[\frac{1}{2}(n+|m|-l)\right]! \left[\frac{1}{2}(n-|m|-l)\right]!} \rho^{n-2l} \quad (5)$$

m and n denote the azimuthal frequency and radial degree, respectively². Due to the non-negative and power-related nature of intensity variations, the use of orthogonal superposition for correction is limited. Therefore, to maximize the correction ability of each mode, the modified intensity Zernike modes are designed to be non-orthogonal. The total number of intensity Zernike modes used in the I-AO corrector is usually determined by the characteristics of the measured sample. For the propose of demonstration, we use the first 15 intensity Zernike modes throughout this work for sensorless I-AO correction. More modes can be applied for more complex aberrations.

Due to the geometrical crosstalk between intensity and phase during SLM modulation, additional phase aberrations will also be introduced. The state of polarisation (SOP) and scalar phase across the SLM can be modelled with Jones calculus to represent the light passing through³⁻⁵. For each point on the pupil plane, the change in SOP and phase can be modelled as:

$$\mathbf{j}_2 = \mathbf{J} \cdot \mathbf{j}_1 \quad (6)$$

where \mathbf{j}_1 and \mathbf{j}_2 are the Jones vectors before and after the change in SOP and scalar phase, respectively, and \mathbf{J} is a 2×2 Jones matrix that models the optical effect of an SLM sandwiched between a pair of crossed polarisers. In this paper, we focus exclusively on retardance and phase modulation for fully polarised light. As a result, \mathbf{J} can be expressed as

$$\mathbf{J} = e^{i\phi} \cdot \mathbf{U} \quad (7)$$

where ϕ is the scalar phase applied to the SLM and \mathbf{U} is a special unitary matrix (SU) describing the change in SOP. This latter matrix can also be parametrised as⁶

$$\mathbf{U} = SU2(\mathbf{Q}, \phi) = \cos\left(\frac{\phi}{2}\right) \mathbf{I} + \sin\left(\frac{\phi}{2}\right) \cdot (n_1 \sigma_1 + n_2 \sigma_2 + n_3 \sigma_3) \quad (8)$$

where \mathbf{I} is the 2×2 identity matrix, and $\sigma_1, \sigma_2, \sigma_3$ are the Pauli matrices defined as

$$\sigma_1 = \begin{bmatrix} 1 & 0 \\ 0 & -1 \end{bmatrix}, \sigma_2 = \begin{bmatrix} 0 & 1 \\ 1 & 0 \end{bmatrix}, \sigma_3 = \begin{bmatrix} 0 & i \\ -i & 0 \end{bmatrix} \quad (9)$$

Note that σ_3 is defined differently than that in some other sources^{3-5,7,8}. Here, the coefficients n_1, n_2, n_3 belong to a vector $\mathbf{Q} = [n_1, n_2, n_3]$ with unit norm, i.e., $\|\mathbf{Q}\| = 1$. The SLM, which is based on a nematic liquid crystal (NLC), exhibits a phase delay between its two optical axes. This delay is governed by its birefringence, Δn , which can be modulated by an external electric field. In the SLM, the phase delay introduced by each pixel is determined by the pixel value applied and is defined as:

$$\phi = \frac{2\pi \cdot \Delta n \cdot d}{\lambda} = 2\arcsin\left(\sqrt{\frac{T}{\sin^2 2\chi}}\right) \quad (10)$$

where the definition of $T, \chi, \Delta n, d$ and λ follows the definition as described in **Supplementary Note 2** and the phase delay ϕ is controlled by the pixel values. The effect of a single pixel on the SLM can then be expressed by

$$J_{LC} = \begin{bmatrix} e^{i\phi} & 0 \\ 0 & 1 \end{bmatrix} = e^{i\frac{\phi}{2}} \begin{bmatrix} e^{i\frac{\phi}{2}} & 0 \\ 0 & e^{-i\frac{\phi}{2}} \end{bmatrix} = e^{i\frac{\phi}{2}} \cdot SU2(\mathbf{H}, \phi) \quad (11)$$

where $\mathbf{H} = [1; 0; 0]$. In our experiment, the SLM is configured with a reflective backplane behind the pixel array. Consequently, the Jones vector after reflection from the SLM can be expressed as:

$$J_{SLM} = J_r \cdot e^{i\frac{\phi}{2}} \cdot SU2(\mathbf{H}, \phi) \quad (12)$$

where $J_r = \sigma_1 = iSU2(\mathbf{H}, \pi)$ represents the reflection from the backplane of the SLM⁹. The Jones matrices for linear polarisers at $+45^\circ$ and -45° are given, respectively, by

$$J_{+45} = \frac{1}{2} \begin{bmatrix} 1 & 1 \\ 1 & 1 \end{bmatrix} \quad (13)$$

$$J_{-45} = \frac{1}{2} \begin{bmatrix} 1 & -1 \\ -1 & 1 \end{bmatrix} \quad (14)$$

Therefore, the Jones matrix of each pixel across the pupil of the SLM module is represented as:

$$J = J_{-45} \cdot J_{SLM} \cdot J_{+45} \quad (15)$$

This relationship leads to the input and output Jones vectors before and after SLM modulation:

$$\mathbf{j}_2 = J_{-45} \cdot J_{SLM} \cdot J_{+45} \cdot \mathbf{j}_1 = e^{i\frac{\phi+\pi}{2}} \cdot J_{+45} \cdot SU2(\mathbf{H}, \phi)SU2(\mathbf{H}, \pi) \cdot J_{-45} \cdot \mathbf{j}_1 \quad (16)$$

Subsequently, the phase difference between \mathbf{j}_1 and \mathbf{j}_2 is computed using the Pancharatnam connection^{8,10}, which we define as

$$\Pi(\mathbf{j}_1, \mathbf{j}_2) = \arg(\mathbf{j}_1^\dagger \mathbf{j}_2) \quad (17)$$

The DM then compensates for this additional phase by applying $\varphi = -\Pi(\mathbf{j}_1, \mathbf{j}_2)$. Based on the intensity Zernike pattern $T = Z_n^m(\rho, \theta)$ applied to the SLM, the corresponding phase φ can be derived from **Equation 16** and **Equation 17** with a range between $[0.5\pi, \pi]$. Therefore, each intensity Zernike pattern applied onto the SLM will have a companion DM phase pattern to ensure that the I-AO corrector provides pure intensity modulation. The combined use of an SLM with crossed polarisers and a DM forms the foundation of this I-AO sensorless algorithm. The first 15 modified intensity Zernike modes are demonstrated alongside their corresponding phase Zernike mode in **Figure S4**.

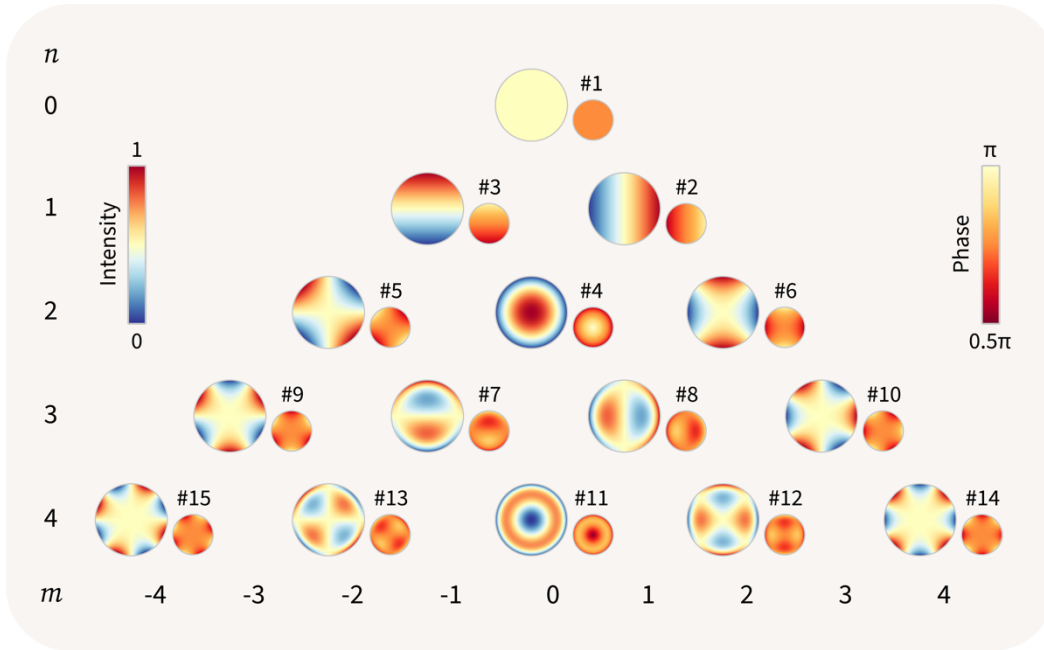


Figure S4: The first 15 modified intensity Zernike modes (left) demonstrated alongside their corresponding phase Zernike mode (right). m and n denote the azimuthal frequency and radial degree, respectively. Intensity Zernike modes range between $[0, 1]$, and the additional phase aberrations introduced by the SLM range between $[0.5\pi, \pi]$, as shown by the colour bar on the right. The indexing of intensity Zernike modes adheres to the Noll's convention.

Supplementary Note 5:

Experimental procedures for sensorless I-AO

Our sensorless I-AO technique iteratively applies predefined patterns to the I-AO corrector to correct for intensity aberrations detected at the focal plane. This method is inspired by established wavefront sensorless algorithms for phase aberration correction AO in microscopy. The key distinction between the sensorless and sensor-based approach is that the former relies on evaluating the FID profile at the focal plane to infer the aberration indirectly, as it cannot directly measure the intensity profile from the pupil plane. In addition, instead of using traditional phase AO Zernike modes, the modified set of intensity Zernike modes discussed in **Supplementary Note 4** is employed for intensity aberration correction.

Initially, by following the SLM calibration procedures outlined in **Supplementary Note 2**, the SLM is configured to have a uniform intensity level measured with the monochromatic camera. Subsequently, an arbitrary intensity aberration is introduced, distorting the FID. In the first correction loop, we evaluate 21 intensity Zernike modes to identify the optimal mode and coefficient that restores beam uniformity. However, intensity Zernike modes mentioned in **Supplementary Note 4** do not support super-positioning in the same way traditional Zernike modes do in phase correction. Our method performs a coarse scan through the coefficient range $[0,1]$ for each mode with a step size of 0.2 and captures an FID profile for each step, followed by resetting the I-AO corrector to a flat state prior to examining the subsequent mode. By contrast, conventional phase AO sensorless algorithms retain the optimal coefficients of previous modes on the AO device during subsequent scans. The approach of releasing the previous correction mode before applying the next avoids intensity saturation at the pupil plane.

To select the optimal mode and coefficient for aberration correction, we assess FID profile images from the coarse scan and focus on the quality of the focal spot. The goal is to find the intensity Zernike mode and coefficient that restores a standard Airy disk shape. Selection relies on two criteria: the low spatial frequency content of FID profile images¹¹ and focal spot circularity. The low spatial frequency criterion identifies the coefficient of a certain mode closest to the ideal intensity profile, and circularity determines if the selected mode and coefficient restores the focus to the desired shape. The circularity C is computed as

$$C = \frac{4A\pi}{P^2} \quad (18)$$

where A is the spot area and P is the perimeter of the target spot. Circularity values of 1 indicate a perfect circle, with larger deviations from 1 reflecting a poorer FID profile. During experiments, an optimal coefficient is first determined for each mode using the low spatial frequency algorithm. Then a circularity C is calculated for each instance and the mode that offers the value of C closest to 1 is selected. This forms the mode selection criterion. Finally, of all the modes that provide a C value close to 1, the mode with the lowest index number is selected for simplicity. For proof-of-concept demonstration stage, only the best mode is selected for correction. However, in principle, this method can be used to correct multiple modes sequentially, provided that the combination of these modes does not cause the intensity level to saturate.

After identifying the optimal mode for aberration correction, its coefficients are rescanned between $[0,1]$ with a fine increment of 0.05, and FID profile images for each coefficient are captured and analysed the low spatial frequency content to identify the optimal coefficient. The selected mode and coefficient are then applied, and an image is captured at the focal plane for validation. Any residual discrepancy between the actual and ideal focal spot profile is attributed to phase aberrations incurred when applying the intensity aberration correction pattern onto the SLM. Consequently, the conventional sensorless phase AO is applied to address these remaining phase aberrations, resulting in an improved FID profile.

Following the initial correction loop that restores intensity profile uniformity using the selected mode and coefficient, a second correction loop is initiated to recover the total beam intensity, which is accomplished by adjusting the ND filter after the laser source. The entire sensorless correction workflow is depicted in the flowchart provided in **Figure S5**.

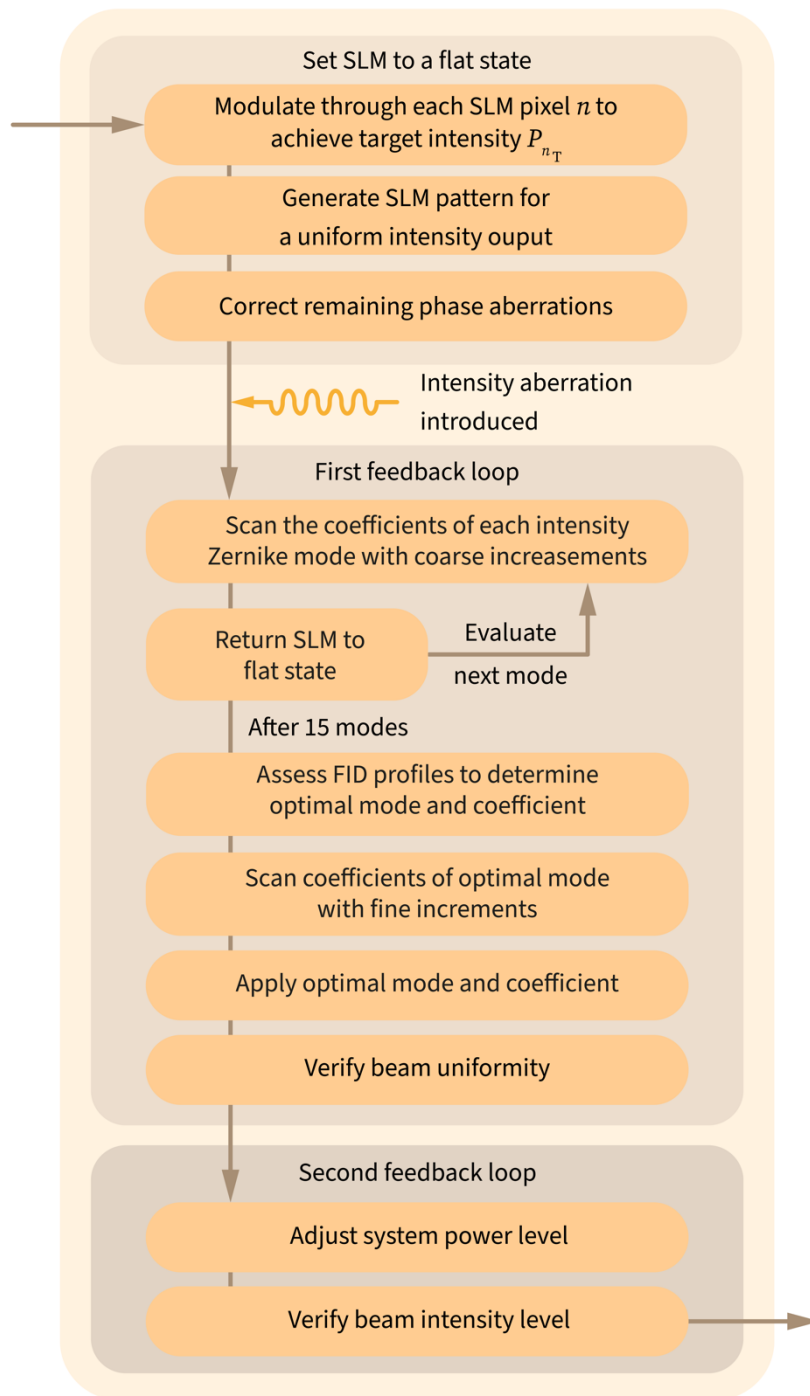


Figure S5: Detailed flowchart of the sensorless I-AO pipeline. The steps include initial SLM calibration, iterative application and evaluation of intensity Zernike modes, and final adjustments to restore both intensity uniformity and total intensity.

Reference

- [1] Dai, Y., Antonello, J., & Booth, M. J. Calibration of a phase-only spatial light modulator for both phase and retardance modulation. *Opt. Express* **27**, 17912–17926 (2019).
- [2] Lakshminarayanan, V. & Fleck, A. Zernike polynomials: a guide. *J. Mod. Opt.* **58**, 545–561 (2011).
- [3] Chipman, R., Lam, W.S.T., & Young, G. *Polarized Light and Optical Systems* (CRC Press, 2018).
- [4] Theocaris, P. S. & Gdoutos, E. E. *Matrix theory of photoelasticity* (Springer, 2013).
- [5] Goldstein, D. H. *Polarized light* (CRC Press, 2011).
- [6] Steane, A. M. An introduction to spinors. Preprint on: <https://doi.org/10.48550/arXiv.1312.3824> (2013).
- [7] Carl, M. Influence of polarization aberrations on point images. *J. Opt. Soc. Am. A* **34**, 967–974 (2017).
- [8] Gutiérrez-Vega, J. C. Pancharatnam–Berry phase of optical systems. *Opt. Lett.* **36**, 1143–1145 (2011).
- [9] He, C., Antonello, J. & Booth, M.J. Vectorial adaptive optics. *eLight* **3**, 23 (2023).
- [10] Pancharatnam, S. Generalized theory of interference and its applications. *Proc. Indian Acad. Sci.* **44**, 398–417 (1956).
- [11] Debarre, D., Booth, M. J. & Wilson, T. Image based adaptive optics through optimisation of low spatial frequencies. *Opt. Express* **15**, 8176-8190 (2007).